Distribution of Random-Flight Chains in Solution near Convex Barriers

Edward F. Casassa

Department of Chemistry, Carnegie Mellon University, Pittsburgh, Pennsylvania 15213

Received August 6, 1996; Revised Manuscript Received January 2, 1997⊗

ABSTRACT: Equilibrium distributions of random-flight linear polymer chains in solution near impenetrable convex barriers are derived for two models: a sphere and a long circular cylinder immersed in the polymer solution. As was shown earlier for chains restricted to one side of an infinite plane interface, the entropic repulsion due to the constraint on chain conformations causes a redistribution of chain segments, with interior segments being more strongly rejected than chain ends as the total segment concentration vanishes at the interface. As the polymer chain length increases, the segment distribution at the interface becomes progressively dependent on the curvature of the boundary, and significant differences in the polymer segment distributions develop among the models. For long chains about a sphere, segment concentration profiles (normalized to unit concentration in the bulk phase) are asymptotically independent of chain length, whereas no such limit is found for the plane or cylinder. The most noticeable feature of segment profiles for long chains about a cylinder is that the concentration of chain ends is nearly proportional to the logarithm of the radial distance from the cylinder axis over a surprisingly large distance range, which increases with chain length. The average thickness of the "depletion layer" at the spherical and cylindrical interfaces is calculated and correlated with chain length and curvature of the barrier. Finally, the segment distribution of star-shaped branched chains at the spherical interface is discussed briefly.

Introduction

Flexible polymer chains in solution are repelled from a passive but impenetrable interface because restrictions on chain conformations near the barrier create an entropically unfavorable environment. In earlier papers we discussed in detail the distribution of random-flight chains in the resulting "depletion layer" at a plane interface, wherein the equilibrium chain-segment concentration increases from zero at the barrier to the concentration of the bulk phase away from the barrier.[1,2] We presented analytical and numerical results showing how the segment distribution varies with position along the chain, interior segments being more strongly repelled from the interface than chain ends, and we also calculated averaged segment density profiles for both linear chains and star-shape branched models.

Here we consider the distribution of random flights in the vicinity of convex interfaces—specifically for a sphere and for a circular cylinder surrounded by a solution medium of indefinite extent. Thus we have idealized models for a spherical colloid and for a fiber immersed in a polymer solution under Θ conditions. As in the earlier work, the first objective is to find solutions of the diffusion equation subject to the appropriate initial and boundary conditions, and as before, in doing this we can profit from formal analogies with results gleaned from the abundant literature on problems in heat conduction. We will have occasion below to refer to the standard treatise on that subject by Carslaw and Jaeger (CJ).[3]

Most of the following discussion concerns linear polymer chains, but at the end we derive some simple results on star-shaped branched polymers at a spherical interface.

Polymer Solution Surrounding an Impenetrable Sphere

Considering a population of linear random-flight chains, each of n statistical segments, about a sphere of radius a, we rewrite eq A2 in the Appendix, denoting the probability explicitly as a relative number density (concentration) $\rho_0(s)$ of chain ends at distance r from the center of the sphere in terms of the dimensionless variable $s = r/a$:

$$\rho_0(s) = 1 - \frac{1}{s}\,\mathrm{erfc}\left(\frac{s-1}{2\sigma}\right) \tag{1}$$

in the domain $1 \le s \le \infty$. Here $\sigma = R_g/a = (nb^2/6a^2)^{1/2}$ represents a relative chain length, R_g being the root-mean-square (rms) radius of gyration of the unconfined chain with rms segment length b. The erfc(x) function is the error function complement [1 − erf(x)]. The concentration is normalized so that $\rho_0(\infty) = 1$.

To obtain segment density profiles for chain segments other than the ends, we need to consider the simultaneous generation of two linear chains (or subchains), one of m segments and the other of $m - n$ segments at any point at distance r. Since the two random flights are independent, save for their common starting point, the probability of success in avoiding impingement on the sphere is a product of two terms like the right-hand side of eq 1. We express the segment numbers m and n in terms of a continuous variable $u = m/n$ and write for the segment density due to the population of mth segments:

$$\rho(s,u) = \left[1 - \frac{1}{s}\,\mathrm{erfc}\left(\frac{s-1}{2\sigma\sqrt{u}}\right)\right]\left[1 - \frac{1}{s}\,\mathrm{erfc}\left(\frac{s-1}{2\sigma\sqrt{1-u}}\right)\right] \tag{2}$$

It is obvious that $\rho(s,u) = \rho(s,1-u)$ and $\rho_0(s) = \rho(s,0) = \rho(s,1)$.

Some characteristics of the density profiles are easily deduced. As in the case of a plane barrier, the initial dependence of the end-segment profile on s (or r) as s approaches unity is linear since differentiation of eq 1

⊗ Abstract published in *Advance ACS Abstracts,* February 15, 1997.

S0024-9297(96)01185-0 CCC: $14.00

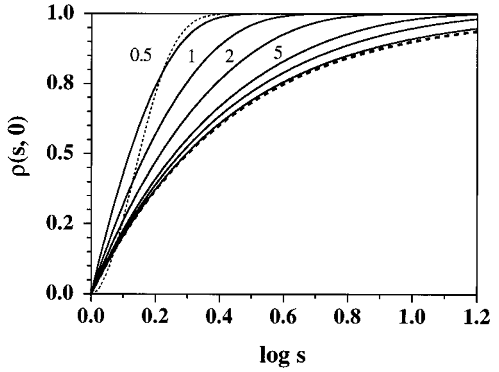

Figure 1. End-segment density profiles for random-flight polymer chains in solution near an impenetrable sphere: relative chain size $\sigma = 0.5$, 1, 2, 5, 10, 50 (from left to right, continuous curves). The bold dashed curve is the asymptotic limit for $\sigma = \infty$. The middle-segment profile for $\sigma = 0.5$ (dotted curve) is added for comparison.

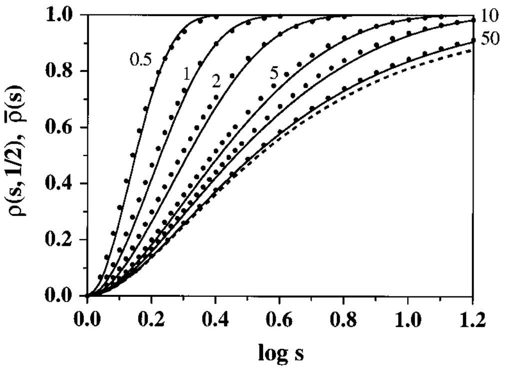

Figure 2. Middle-segment density profiles for the sphere model: $\sigma = 0.5$, 1, 2, 5, 10, 50 (from left to right, continuous curves) The dashed curve is the asymptotic limit for $\sigma = \infty$. Circles show the averaged profile $\bar{\rho}(s)$ for the respective values of σ.

gives

$$\lim_{s\to 1}\left(\frac{d\rho_0(s)}{ds}\right) = 1 + \frac{1}{\sigma\sqrt{\pi}} \qquad (3)$$

On the other hand, when $u \neq 0, 1$, the first derivative vanishes, and the Taylor's series expansion of $\rho(s,u)$ about $s = 1$ begins with

$$\rho(s,u) = \frac{1}{2}(s-1)^2 \lim_{s\to 1}\left(\frac{\partial^2\rho(s,u)}{\partial s^2}\right) + \ldots$$
$$= \left(1 + \frac{1}{\sigma\sqrt{\pi u}}\right)\left(1 + \frac{1}{\sigma\sqrt{\pi(1-u)}}\right)(s-1)^2 + \ldots \qquad (4)$$

i.e. the initial dependence on $s - 1$ is quadratic.

The solid curves in Figures 1 and 2 show, respectively, $\rho(s,0)$ and $\rho(s,0.5)$ plotted against log s (base 10) for $\sigma = 0.5$, 1, 2, 5, 10, 50. If the sphere radius a is considered fixed, the succession of curves shows, on a common distance scale, the effect of increasing chain length σ on the density profiles. The disparity between the end-segment and middle-segment profiles increases markedly with increasing σ. It is interesting that the density profiles at large σ asymptotically become independent of σ: i.e. $1 - 1/s$ for end segments and $(1 - 1/s)^2$ for middle segments. In both cases, the profile for $\sigma = 50$ is already close to the asymptotic curve. Furthermore, since the erfc functions in eq 2 tend to unity for large σ with any $u \neq 0, 1$, it is evident that the asymptotic profiles are the same for all interior segments. It follows that the profiles for interior segments become more alike with increasing σ.

The initial slope $d\rho(s,0)/ds$ according to eq 3 decreases with increasing chain length σ, but not without limit, approaching unity asymptotically. This limit corresponds to $d(1 - 1/s)/ds$ at $s = 1$.

The overall segment density profile, normalized to unity at large s, is given by the average

$$\bar{\rho}(s) = \int_0^1 \rho(s,u)\, du = 2\int_0^{1/2} \rho(s,u)\, du \qquad (5)$$

with the $\rho(s,u)$ function of eq 2. It appears that this integral cannot be expressed in terms of elementary functions, but numerical integration provided the points for $\bar{\rho}(s)$ plotted as circles in Figure 2. Obviously, the averaged profile is generally close to the middle-segment profile and has to merge with it as $\sigma \to \infty$. Even apart from its unique finite slope as $s \to 1$, the shape of the end-segment profile represents the extreme deviation of any profile $\rho(s,u)$ from $\bar{\rho}(s)$.[4]

An expression for $\bar{\rho}(s)$ for s near unity is obtained by integrating eq 4 with respect to u to obtain

$$\bar{\rho}(s) = \left(1 + \frac{4}{\sigma\pi^{1/2}} + \frac{1}{\sigma^2}\right)(s-1)^2 + \ldots \qquad (6)$$

The ratio

$$\lim_{s\to 1}\left[\frac{\rho(s,1/2)}{\bar{\rho}(s)}\right] = \left(1 + \frac{2^{1/2}}{\sigma\pi^{1/2}}\right)^2 \Big/ \left(1 + \frac{4}{\sigma\pi^{1/2}} + \frac{1}{\sigma^2}\right) \qquad (7)$$

affords a comparison of the middle-segment profile $\rho(s,1/2)$ with $\bar{\rho}(s)$ as $s \to 1$. For short chains ($\sigma \to 0$) the ratio is $2/\pi = 0.6366$; it increases to unity as $\sigma \to \infty$. For any σ, this ratio probably represents the maximum fractional deviation of $\rho(s,1/2)$ from $\bar{\rho}(s)$.

The total deficit of mth segments in the depletion layer is given by the integral of $[1 - \rho(s,u)]$ over the volume of the region $r > a$:

$$\int_1^\infty \left\{1 - \left[1 - \frac{1}{s}\operatorname{erfc}\left(\frac{s-1}{2\sigma\sqrt{u}}\right)\right] \times \left[1 - \frac{1}{s}\operatorname{erfc}\left(\frac{s-1}{2\sigma\sqrt{1-u}}\right)\right]\right\} 4\pi s^2\, ds = \int_1^\infty \operatorname{erfc}\left(\frac{s-1}{2\sigma}\right) 4\pi s\, ds = 4\pi\left(\frac{2\sigma}{\sqrt{\pi}} + \sigma^2\right) \qquad (8)$$

This integral is independent of u since deleting any segment of a forbidden chain configuration necessarily eliminates from the accounting every other segment of the chain.[1] The average thickness of the depletion layer can be computed as the thickness of an annular region between $r = a$ and $r_d = as_d$ that, if it were empty of polymer, would account for the total deficit of segments in the depletion layer, i.e.

$$\frac{4}{3}\pi({s_d}^3 - 1) = \int_1^\infty [1 - \rho(s,u)] 4\pi s^2\, ds \qquad (9)$$

so that, with eq 8, we have

$$s_d = \left(1 + \frac{6\sigma}{\sqrt{\pi}} + 3\sigma^2\right)^{1/3} \qquad (10)$$

The thickness of the depletion layer in units of a is $\Delta s_d = s_d - 1$.

Polymer Solution Surrounding an Impenetrable Cylinder

Just as the segment density profile of chain ends about a sphere could be inferred from an equation from heat conduction theory, a simple transformation of eq A4 in the Appendix gives the result we need for the end-segment concentration profile about an impenetrable circular cylindrical fiber of radius a and infinite length in a polymer solution at the Θ point:

$$\rho_0(s) = \frac{2}{\pi}\int_0^\infty e^{-\sigma^2 x^2}\,\Phi(s,x)\,\frac{dx}{x} \qquad (11)$$

in which

$$\Phi(s,x) = \left[\frac{J_0(x)\,Y_0(sx) - Y_0(x)\,J_0(sx)}{J_0^{\,2}(x) + Y_0^{\,2}(x)}\right] \qquad (12)$$

Here, $J_0(x)$ and $Y_0(x)$ denote Bessel functions of the first and second kinds, respectively, of order zero. Similarly to our relation for the sphere model, the radial distance r is expressed in terms of $s = r/a$; and the polymer size, by $\sigma = R_g/a$. It appears that the integral has to be evaluated numerically; and since $\Phi(s,x)$ is a damped oscillatory function that has an infinity at $x = 0$, care is required in the computation. Procedures that yield numerical results with six significant digits for $\rho_0(s)$ and related integrals for the cylinder model are described in some detail in the Appendix.

To find the initial slope of the profile of an end segment, we differentiate eq 11 with respect to s and utilize a property of Bessel functions,

$$J_0(z)\,\frac{dY_0(z)}{dz} - Y_0(z)\,\frac{dJ_0(z)}{dz} = \frac{2}{\pi z} \qquad (13)$$

to obtain

$$\lim_{s\to 1}\left[\frac{d\rho_0(s)}{ds}\right] = \frac{4}{\pi^2}\int_0^\infty \frac{e^{-\sigma^2 x^2}}{J_0^{\,2}(x) + Y_0^{\,2}(x)}\,\frac{dx}{x} = \frac{4}{\pi^2} I_{JC}(\sigma) \qquad (14)$$

We designate this integral as $I_{JC}(\sigma)$ because Jaeger and Clarke[5,6] discussed it in the context of heat transfer and tabulated approximate values. The integrand of I_{JC} is a positive quantity that decreases monotonically from a singularity at $x = 0$ to zero as σ tends to infinity. For σ finite, the nonvanishing first derivative implies that $\rho_0(s)$ is initially linear in s.

Figure 3 shows end-segment profiles $\rho_0(s)$ for the cylinder model with several values of σ.[7,8] As in the case of the sphere, we make the abscissa log s. This allows the profiles for a wide range of chain lengths to be compared and also exhibits a notable feature of these functions—that $\rho_0(s)$ appears to be proportional to the logarithm of s over surprisingly wide ranges. The initial slope of a plot in this representation is given by

$$\lim_{s\to 1}\left[\frac{d\rho_0(s)}{d\ln s}\right] = \lim_{s\to 1}\left[s\,\frac{d\rho_0(s)}{ds}\right] = \frac{4}{\pi^2} I_{JC}(\sigma) \qquad (15)$$

according to eq 14, but it is evident that the slope remains sensibly constant for s far beyond the $s = 1$ limit. The limiting behavior of $\rho_0(s)$ is just

$$\rho_0(s)_{\text{appr}} = \lim_{s\to 1}\,[\rho_0(s)] = \frac{4}{\pi^2} I_{JC}(\sigma)\ln s \qquad (16)$$

and to the extent that the end-segment plots in Figure 3 are linear, eq 16 actually remains a good approximation away from the limit $s = 1$ when the relative chain size σ is large. Figure 4 shows deviations of the approximation $\rho_0(s)_{\text{appr}}$ from the exact function $\rho_0(s)$ for the values of σ used in Figure 3.

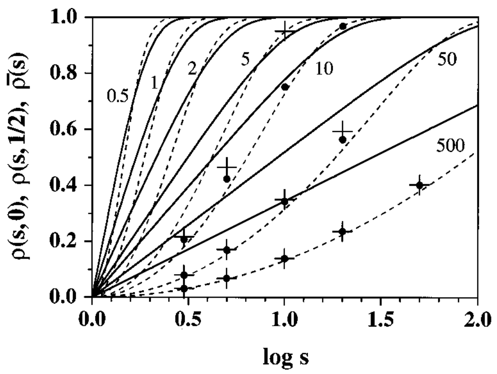

Figure 3. Density profiles for the cylinder model: end segments (solid curves) and middle segments (dashed curves). Values of σ are marked on the plots (where possible near the point of intersection of end-segment and middle-segment curves) for each σ. The points represent values of $\bar{\rho}(s)$ from eq 23 (filled circles) and the corresponding approximation from eq 24 (crosses) for $\sigma = 10, 50, 500$.

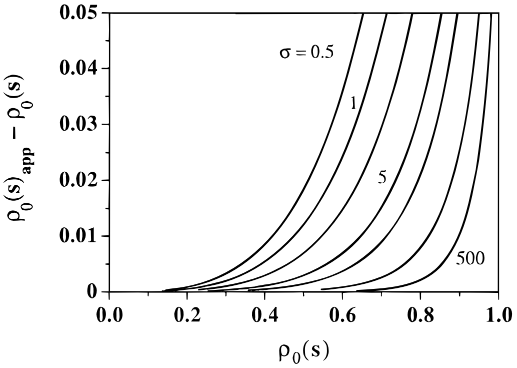

Figure 4. Deviation of the approximate end-segment profile according to eq 16 from the true value for $\sigma = 0.5, 1, 2, 5, 10, 50, 500$ (curves from left to right).

For large σ, an asymptotic series representation for I_{JC} is[6] (CJ, p 336):

$$I_{JC}(\sigma) \sim I_{JC}(\sigma)_\infty$$

$$= \frac{\pi^2}{2}\left\{\frac{1}{\ln(4\sigma^2) - 2\gamma} - \frac{\gamma}{[\ln(4\sigma^2) - 2\gamma]^2} - \ldots\right\} \qquad (17)$$

where γ is Euler's constant 0.577 22.... The asymptotic behavior of $\rho_0(s)$ in the range of distance s where eq 17 applies is thus

$$\lim_{s\to 1}\,[\rho_0(s)] \sim 2\,(\ln s) I_{JC}(\sigma)_\infty \qquad (18)$$

For values of σ where it is meaningful, the two-term approximation in eq 17 is greater than I_{JC}; the ratio $I_{JC}(\sigma)_\infty/I_{JC}(\sigma)$ is 1.197, 1.094, 1.054, 1.020, 1.008, respectively, for $\sigma = 2, 5, 10, 50, 500$. Equations 17 and 18 show that the end-segment profiles for the cylinder model (unlike eq 1 for the sphere) do not approach a finite asymptotic form at large σ. The same assertion can be extended to all segments since, as is shown below, the integral I_{JC} is similarly involved in the limiting forms for density profiles of interior segments.

As before, we obtain the density profile for an interior segment of a chain of n segments as the joint probability of success in generating subchains of lengths $m = un$ and $n - m = (1 - u)n$ from a common point. The result is

$$\rho(s,u) = \frac{4}{\pi^2}\int_0^\infty e^{-u\sigma^2x^2}\,\Phi(s,x)\,\frac{dx}{x} \times \int_0^\infty e^{-(1-u)\sigma^2x^2}\,\Phi(s,x)\,\frac{dx}{x} \tag{19}$$

Profiles for middle segments ($u = {}^1/_2$) are shown in Figure 3 for comparison with the end-segment profiles. In common with the sphere model discussed above, the density profile for any interior segment becomes quadratic in $s - 1$ (and in ln s) as $s \rightarrow 1$. Furthermore, when the approximation in eq 16 can be applied to both the subchains joined by the mth segment of the chain, we have

$$\rho(s,u) \approx \left(\frac{4}{\pi^2}\right)^2\{I_{JC}[u^{1/2}\sigma]\, I_{JC}[(1-u)^{1/2}\sigma]\}(\ln s)^2 \tag{20}$$

and, in particular, for the middle-segment profile

$$\rho(s,0.5) \approx \left(\frac{4}{\pi^2}\right)^2[I_{JC}(\sigma/2^{1/2})]^2(\ln s)^2 \tag{21}$$

so that plots of $\rho(s,u)$ for the middle-segment functions in Figure 3 would appear linear over a finite span of s when plotted against (log s)^2.

The averaged density profile for the cylinder model can be written

$$\bar\rho(s) = \int_0^1 \rho(s,u)\,du = \frac{4}{\pi^2}\int_0^1\left[\int_0^\infty\int_0^\infty e^{-u\sigma^2x^2-(1-u)\sigma^2y^2}\,\Phi(s,x) \times \Phi(s,y)\,\frac{dx}{x}\,\frac{dy}{y}\right]du \tag{22}$$

The integration over u is easy:

$$\bar\rho(s) = \frac{4}{\pi^2}\int_0^\infty\int_0^\infty \frac{e^{-\sigma^2x^2} - e^{-\sigma^2y^2}}{\sigma^2y^2 - \sigma^2x^2}\,\Phi(s,x)\,\Phi(s,y)\,\frac{dx}{x}\,\frac{dy}{y} \tag{23}$$

but the remaining double integral cannot be evaluated analytically. The first factor of the integrand appears indeterminate when $x = y$, and the difficulties connected with the oscillatory functions $\Phi(s,x)$ and $\Phi(s,y)$, which go to infinity as x, $y = 0$, are compounded in the double integral. The procedure described in the Appendix for evaluating these double integrals was used to obtain values of $\bar\rho(s)$ shown in Table 2 and in Figure 3.

Table 1. Parameters Characterizing Segment Density Profiles for Linear Chains near a Cylinder

σ	I_{JC}[a]	I_2[b]	$\lim_{s\to1}[\rho(s,0.5)/\bar\rho(s)]$
0.1	15.122 48		
0.2	8.134 558		
0.5	3.893 609		
1	2.427 358	13.205 276	0.701 546
2	1.639 334	5.268 348	0.740 561
5	1.088 765	1.968 712	0.799 505
10	0.852 635	1.092 091	0.840 019
20	0.695 886	0.674 000	0.872 518
50	0.557 252	0.402 501	0.903 224
100	0.483 443	0.291 649	0.919 331
200	0.426 569	0.220 622	0.931 235
500	0.368 917	0.160 367	0.942 719
1000	0.350 930	0.129 157	0.953 505

[a] Data taken from 37 points calculated in the range 0.1 ≤ 1000 with nine points in each logarithmic decade of σ. A regression fit of the full set is

$$\log I_{JC} = 0.388043 - 0.607854 \log\sigma + 0.171277(\log\sigma)^2 - 0.021653(\log\sigma)^3 \qquad R^2 = 0.999\,944$$

[b] These data are fitted by

$$\log I_2 = 1.118579 - 1.427580 \log\sigma + 0.395535(\log\sigma)^2 - 0.047696(\log\sigma)^3 \qquad R^2 = 0.999\,980$$

Table 2. Comparison of $\bar\rho(s)$, $\bar\rho(s)_{appr}$, and $\rho(s,0.5)$ for the Cylinder Model

σ	s	$\bar\rho(s)$	$\bar\rho(s)_{appr}$	$\rho(s,0.5)$
10	3	0.207 319	0.216 505	0.181 004
	5	0.423 003	0.464 652	0.382 898
	10	0.751 234	0.951 066	0.727 281
	20	0.961 222	1.609 85	0.968 493
50	3	0.079 540	0.079 795	0.072 064
	5	0.170 026	0.171 252	0.154 598
	10	0.343 759	0.350 524	0.315 740
	20	0.564 057	0.593 325	0.529 280
500	3	0.031 791	0.031 792	0.029 971
	5	0.068 227	0.068 231	0.064 323
	10	0.139 616	0.139 658	0.131 656
	20	0.236 166	0.236 396	0.222 837
	50	0.401 495	0.403 123	0.379 813

The approximate form for $\bar\rho(s)$ consistent with $\rho(s,u)$ given by eq 20 involves a somewhat simpler double integral:

$$\bar\rho(s) \approx \bar\rho(s)_{appr} = \frac{16}{\pi^4}(\ln s)^2\, I_2(\sigma) \tag{24}$$

where

$$I_2(\sigma) = \int_0^\infty\int_0^\infty \frac{e^{-\sigma^2x^2} - e^{-\sigma^2y^2}}{\sigma^2y^2 - \sigma^2x^2}\,\varphi(x)\,\varphi(y)\,\frac{dx}{x}\,\frac{dy}{y} \tag{25}$$

with

$$\varphi(x) = 1/[J_0^{\,2}(x) + Y_0^{\,2}(x)] \tag{26}$$

Thus a single value of $I_2(\sigma)$ suffices for calculating values of $\bar\rho(s)$ for a given σ over the range of s where eq 24 is an acceptable approximation. The computational procedure we used for $I_2(\sigma)$ is described in the Appendix. The fact that the integrand of eq 25 lacks the oscillatory behavior of $\Phi(s,x)$ and $\Phi(s,y)$ considerably simplifies computations.

Although we cannot write an algebraic expression for the ratio of $\rho(s,{}^1/_2)$ to $\bar\rho(s)$ for the cylinder model like eq 7 for the sphere, we can combine eqs 21 and 24 to obtain

$$\left[\frac{\rho(s,1/2)}{\bar\rho(s)}\right] \approx \frac{[I_{JC}(\sigma/\sqrt{2})]^2}{I_2(\sigma)} \tag{27}$$

which becomes exact as $s \rightarrow 1$ and is a close approximation for much of the density profile for long chains. Values given in Table 1 show that this ratio increases with increasing σ, though not as rapidly as in eq 7 for the sphere model, and it is unclear whether it actually tends to unity for large σ. It does appear, however, that the middle-segment profile becomes a better approximation to the averaged density profile as σ increases. In the region of s where the end-segment density is greater than the middle-segment density, we have $\bar{\rho}(s)_{\text{appr}} > \bar{\rho}(s) > \rho_0(s,0.5)$, according to Table 2 and Figure 3. At small σ, $\bar{\rho}(s)_{\text{appr}}$ rapidly diverges from $\bar{\rho}(s)$ as s increases (e.g. for $s = 3$, $\sigma = 10$).

In view of the cylindrical symmetry, the deficit of chains in the depletion layer is measured by integrating $[1 - \rho(s,u)]$ over a cross-section normal to the cylinder, and s_d is obtained from

$$\pi({s_d}^2 - 1) = \int_1^\infty [1 - \rho(s,u)] 2\pi s \, ds \tag{28}$$

with $\rho(s,u)$ given by eq 19; but as in the case of the sphere, the integral on the right-hand side is the same for any value of u, which can thus be chosen for convenience in numerical computation (see Appendix).

Branched Chains

Introduction of chain branching as a structural parameter makes it possible to study variations of chain length and segment distribution, while an overall dimension such as the radius of gyration is held fixed. The f-functional star-branched chain consisting of f linear subchains, each of n segments, connected at a common node is the simplest branching model for analysis, and it is also of practical interest because good approximations to such molecules can be synthesized. Reference 2 is a study of segment distributions of random-flight star chains at a plane interface. In principle, the analysis given there could be generalized to the convex barriers considered here.[9] However, without undertaking a detailed treatment, we can deduce directly some results for the special case of the distribution of the branch nodes. The basic question is, what is the probability of generating f random-flight linear chains, each with n segments, from a point at reduced distance s from the center of a sphere or cylinder, without intersecting its surface? The obvious answer is that we need only multiply the end-segment probability for a linear chain of n segments by itself f times.

Accordingly, the density distribution of branch nodes about a sphere is

$$\rho_{\text{node}}(s) = \left[1 - \frac{1}{s} \operatorname{erfc}\left(\frac{s-1}{2\sigma}\right)\right]^f \tag{29}$$

where, as before, $a\sigma$ is the rms radius of gyration of the linear chain of n units and $\rho_{\text{node}}(\infty) = 1$. (The "nodes" of degenerate stars with $f = 1, 2$ represent, respectively, the end of an n-segment linear chain and the middle segment of one of length $2n$). The asymptotic behavior of $\rho_{\text{node}}(s)$ is then

$$\rho_{\text{node}}(s) \sim \left(1 - \frac{1}{s}\right)^f \tag{30}$$

The density profile is asymptotically independent of σ, as in the linear-chain case.[10]

The depletion layer thickness for stars, is obtained by substituting $\rho_{\text{node}}(s)$ in eq 9:

$${s_d}^3 = 1 + 3\int_1^\infty \left\{1 - \left[1 - \frac{1}{s} \operatorname{erfc}\left(\frac{s-1}{2\sigma}\right)\right]^f\right\} s^2 \, ds \tag{31}$$

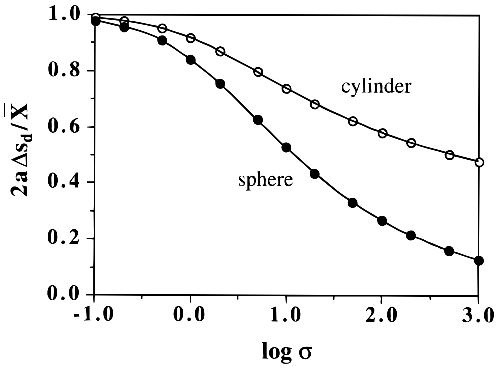

Figure 5. Ratio of depletion layer thickness Δs_d to half the mean projection of the linear random-flight chain for the sphere and cylinder models.

Table 3. Relative Average Thickness of Depletion Layers in Polymer Solution near Spheres and Cylinders

σ	Δs_d (sphere)	Δs_d (cylinder)
0.1	0.110 24	0.111 53
0.2	0.215 77	0.220 66
0.5	0.509 94	0.536 33
1	0.947 39	1.033 86
2	1.703 98	1.962 53
5	3.529 45	4.490 66
10	5.944 12	8.330 07
20	9.825 6	15.428 9
50	18.721 3	34.979 3
100	30.189 1	65.315 4
200	48.417 0	122.624
500	89.924 4	284.209
1000	143.279	539.858

We will not pursue here the question of segment density profiles of branched chains at a cylindrical interface. The relevant expressions analogous to eqs 29 and 31 will be sufficiently evident.

Discussion: Comparison of the Models, Depletion Layer Thickness

In refs 1 and 2, the average thickness of the depletion layer at a plane wall was identified with half the mean projection $\bar{X}$ of the *unconfined* solute molecule, whatever its architecture, onto an axis. For a chain with a given segment (say an end or branch node, etc.) at a given distance from an interface, a convex barrier excludes the chain configurations from less space than does a plane, and consequently, Δs_d for a cylinder or sphere must be less than $\bar{X}/2a$, the sphere giving the smaller value for a common radius. In the short-chain limit ($\sigma \to 0$), the chain effectively "sees" a plane interface in both cases, and Δs_d must approach $\bar{X}/2a$. These trends are demonstrated in Table 1 by values of s_d for linear chains about a sphere and about a cylinder calculated, respectively, from eqs 10 and 28. Using the projection $\bar{X} = (8nb^2/3\pi)^{1/2} = 4R_g/\pi^{1/2}$ for linear chains, we show these data in Figure 5 as ratios

$$\frac{r_d - a}{\bar{X}/2} = \frac{\Delta s_d}{\bar{X}/2a} = \frac{\pi^{1/2}}{2}\left(\frac{\Delta s_d}{\sigma}\right) \tag{32}$$

plotted against log σ.[11]

Even though the segment density profile for linear chains about a sphere is asymptotically independent of the chain length, eq 10 shows that the depletion layer thickness goes to infinity as $\sigma^{2/3}$. Accordingly, since $\bar{X}$ is proportional to σ, the ratio $2a\Delta s_d/\bar{X}$ for the sphere model must tend to zero at large σ, as Figure 5 suggests. If the depletion layer thickness tends to infinity with

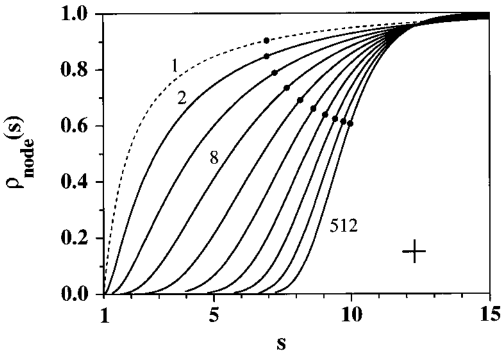

Figure 6. Segment density profiles for nodes of star-branched molecules about a sphere. The branching functionality f is 1, 2, 4, 8, 16, 32, 64,128, 256, and 512. Branch lengths are varied so that all species have the same mean molecular projection (that for an unbranched chain with $\sigma = 10$). The points on the curves mark the density at distance s_d corresponding to the average depletion layer thickness, and the cross marks the common value of the ratio $\bar{X}/2a$.

increasing σ for both plane and sphere models, it is inescapable that it should also tend to infinity for the cylinder model. Although the ratio $2a\Delta s_d/\bar{X}$ for the cylinder (open circles in Figure 5) is seen to decrease rather slowly with increasing log σ it must ultimately vanish. Otherwise we would have to accept the impossible result of an infinitely thin fiber offering an impediment to random flight configurations with a finite number of steps.

Figure 6 presents an illustrative series of node profiles of star chains about a sphere of radius a with branch functionality varying while the mean projection of the chains is held fixed—i.e. as branches are added, the number of segments per branch, hence σ, is decreased to maintain a fixed value of the projection:

$$\bar{X}/a = 4f^{1/2}\sigma\psi(f) \tag{33}$$

where[2]

$$\psi(f) = \left(\frac{f}{\pi}\right)^{1/2}\int_0^\infty [\text{erf } w^{1/2}]^{f-1}\, e^{-w}\, dw \tag{34}$$

When f is 1 or 2, ψ is $1/\pi^{1/2}$. Thus, the profiles for degenerate stars $f = 1$ and $f = 2$ here represent the same linear chain: the dash curve is for an end segment and the other curve is for the middle segment. For $f = 1$, σ is chosen as 10; and this makes $\sigma = 10/2^{1/2}$ for $f = 2$. For the true stars ($f > 2$), chain lengths are scaled similarly according to eq 33. The segment density at distance s_d is marked on each profile. Since the chains with $f = 1$ and $f = 2$ are identical, s_d is the same for these curves. The cross marks the distance from the interface corresponding to $\bar{X}/2$. As the number of branches is increased, the segment density profiles become steeper and appear to approach asymptotically a step function at Δs_d equal to $\bar{X}/2a$. Intuitively, this seems reasonable: stars with many short branches tend toward the behavior of a small solid sphere of radius $\bar{X}/2$ whose center is excluded from a layer of that thickness adjacent to a barrier which is effectively planar with respect to the small sphere.

On the scale of the plot, it appears that the profiles for $f > 1$ intersect at or near $s_d = 1 + \bar{X}/2a$. However, closer scrutiny of the region near this point shows that there is in fact no common intersection, except perhaps as f goes to infinity. Figure 6 can be compared with Figure 4 in ref 1, which shows node-segment profiles for a series of stars with a common mean projection at a plane interface.

Conclusion

The present study continues an examination of random-flight segment density profiles of linear and branched chains at interfaces of various simple geometric forms.[1,2,12] The approach throughout has been to explore what can be done by treating as rigorously as possible very simple models that are amenable to mathematical analysis. Insofar as the models are purely entropic, concerning only geometric constraints on random-flight configuration, we learn nothing of the effects of intermolecular forces that operate in the real system and are the focus of innumerable simulation studies. However, the results can provide useful insights into the entropic effects that must still exist in more realistic systems, even when energetic interactions dominate.

The results on depletion layer thicknesses provide a measure of the effective range of the entropic interactions. Although Δs_d increases less rapidly than $\bar{X}/2a$ as σ is increased, the effect of an impenetrable suspended particle is exerted for a considerable distance if chains are long. When the rms gyration radius of a linear chain is 1000 times the radius a, r_d is still $541a$ for a cylinder and $144a$ for a sphere. The interaction between suspended colloid particles in the presence of free polymer chains has been less studied than the stabilizing effect of adsorbed chains.[13] However, the basic finding is that with free random-flight chains, the entropic affect alone is manifested as a force of attraction between colloids that has a range on the order of chain dimensions.[13,14]

Acknowledgment. I am indebted to Professor J. L. Anderson for stimulating questions and a discussion from which this study developed.

Appendix

Derivation of Equations 1 and 11. In adapting for our purposes heat conduction relations discussed by CJ, it is constructive to consider first the simple problem of the evolution of the temperature T at distance r from the center of a sphere of radius a embedded in a medium $r > a$ initially at uniform temperature T_0. The surface of the sphere is held at zero temperature for all time t (the sphere is a heat sink). From the symmetry of a similar problem solved in CJ for the temperature in a medium initially at zero temperature heated by a sphere with constant surface temperature T_s, it is evident that the result we need is obtained by replacing the ratio T/T_s in CJ eq 9.10.2 (p 247) with $1 - T/T_0$ so that

$$\frac{T}{T_0} = 1 - \frac{a}{r}\,\text{erfc}\left(\frac{r - \text{a}}{\sqrt{4\kappa t}}\right) \tag{A1}$$

The heat conduction model can be interpreted as describing the situation in which identical instantaneous heat sources are placed at uniform density in the region $r > a$ at zero time. The analogous polymer configuration problem is modeled by starting random flights uniformly over $r > a$, allowing them to evolve through n steps, and eliminating any that intersect the spherical boundary. To rewrite eq A1 in the language of the polymer chain model, we have only to make the translations $T/T_0 \rightarrow P_n(r)$, $\kappa \rightarrow b^2/6$, and $t \rightarrow n$:

$$P_n(r) = 1 - \frac{a}{r}\,\mathrm{erfc}\left(\frac{r-a}{\sqrt{2nb^2/3}}\right) \tag{A2}$$

where $P_n(r)$ is the probability that a chain configuration of n steps starting at a point at distance r in $r > a$ can be completed without touching the interface. We can then assert that this probability is proportional to the equilibrium concentration of chain ends at r.

In fact, the "solution by inspection" giving eq A1 (or A2) is easily verified by directly solving the diffusion equation in the form

$$\frac{\partial w}{\partial t} = \kappa\frac{\partial^2 w}{\partial r^2} \qquad w = Tr \tag{A3}$$

with our initial and boundary conditions, by the method of CJ (Chapter 9) or by using the Laplace transformation (CJ, Chapter 12).

Equation 13.5.6 in CJ (p 335) gives the radial temperature distribution in a conducting medium initially at zero temperature, heated by an immersed circular cylinder of radius r with its surface held at constant temperature. By the reasoning indicated above for the sphere model, we can immediately write the correct relation for the temperature T in a medium initially at uniform temperature T_0 including a cylinder with surface temperature held at zero,

$$\frac{T}{T_0} = \frac{2}{\pi}\int_0^\infty e^{-\kappa t x^2}\left[\frac{J_0(x)\,Y_0(ax) - Y_0(x)\,J_0(ax)}{J_0^{\,2}(x) + Y_0^{\,2}(x)}\right]\frac{dx}{x} \tag{A4}$$

without actually having to work through the fairly complicated Laplace transformation for this case. Again the translation $T/T_0 \rightarrow \rho$, $\kappa t \rightarrow nb^2/6$, gives the corresponding end-segment density distribution in the depletion layer about an impenetrable cylinder in a polymer solution.

Numerical Integration. The numerical integrations required to obtain the density profiles appearing in the figures were done with the Mathematica[15] program (Version 2.1) running on a Quadra 700 Macintosh computer. The Mathematica function NIntegrate uses a form of Gaussian quadratures with recursive bisections of the intervals aiming to achieve results valid to 10 significant digits.[15] Depending on the pathology of the integrand, the accuracy actually realized may be far less. Care must be exercised since gross errors may occur, without inciting error messages, if the integration subintervals are too coarse to capture parts of an integrand. Results can be tested for consistency and stability by alternative calculations with different piecewise divisions of the interval of integration (NIntegrate looks for singularities at the end points), or with variations in options such as the number of initial sample points or the maximum number of recursions. Usually, we could refine calculations to the point of having confidence in six significant digits.

Integrations of $\rho(s,u)$ for the sphere with respect to u to obtain $\bar{\rho}(s)$ gave warnings of numeric overflow when u was allowed to vary over the entire interval $0-{}^1/_2$. However, there was no evidence that results were compromised. Making the integration range $\delta \le u \le 1/2$, with δ no greater than 0.000 001, eliminated the overflow message and did not change results recorded to six decimals.

As was expected, calculations with the cylinder model were more refractory. The integrand in eq 11 is a damped oscillatory function of x with a singularity at the origin. The oscillation arises from the numerator of $\Phi(s,x)$:

$$C(s,x) = J_0(x)\,Y_0(sx) - Y_0(x)\,J_0(sx) \tag{A5}$$

which has its nth zero at approximately $x = n\pi/(s-1)$ (a relation which seems to become exact asymptotically for large n). The singularity of $\Phi(s,x)/x$ at the origin is due to

$$\frac{\varphi(x)}{x} = \frac{1}{x}\left[\frac{1}{J_0^{\,2}(x) + Y_0^{\,2}(x)}\right] \tag{A6}$$

which decreases monotonically from infinity to the asymptotic limit $2/\pi$. Initial attempts to evaluate the integral in eq 11 sometimes produced messages warning of convergence failure at small x and/or obviously erratic values for ρ at large s. Such failure became more prevalent at large σ.

The singularity at $x = 0$ cannot simply be avoided since integration to infinity from $x = \delta$, even with $\delta \ll 10^{-6}$, causes much of the integral to be lost. However, doing the integration in two parts, $0 \le x \le \delta$ and $\delta \le x \le \infty$ with δ on the order of $10^{-4}-10^{-7}$ (progressively smaller values being needed at larger values of the parameter σ), leads to correct results for wide ranges of s and σ. Presumably, juggling further subdivisions of the range of integration or increases in the maximum number of recursions set by the computer program would help to achieve convergence.

A more systematic procedure for integration of eqs 11, 14, and 19—one applicable irrespective of the particular capabilities of Mathematica—is desirable; and it is essential for any progress with the related double integrals to be discussed below. We suppose that we are interested in values of σ up to the order of 10^3. Then when x is sufficiently small, the exponential $\exp(-\sigma^2 x^2)$ can be taken as unity. This means that the integral I_{JC} can be divided into two terms:

$$I_{JC} = \int_0^\delta \varphi(x)\,\frac{dx}{x} + \int_\delta^\infty e^{-\sigma^2 x^2}\,\varphi(x)\,\frac{dx}{x} \tag{A7}$$

If δ is taken no larger than 10^{-6}, eq A12 gives I_{JC} correct to at least six significant figures. Since the integrand containing the singularity does not involve σ, it need be evaluated only once and then can be added to values obtained for the second integral. It also turns out that the Bessel functions in $\varphi(x)$ can be represented over the range of δ by the leading terms of their series expansions:

$$\lim_{x\to 0}\,[\varphi(x)] = \varphi_0(x) = \left[1 + \frac{4}{\pi^2}\left(\ln\frac{x}{2} + \gamma\right)^2\right]^{-1} \tag{A8}$$

where $\gamma = 0.577\,216...$ is Euler's constant. The integral of $\varphi_0(x)/x$ is smaller than the correct integral of $\varphi(x)/x$, but by no more than 4 parts in 10^8 when δ is taken no larger than 10^{-3}. In fact, this integration can be done analytically:[16]

$$\int_0^\delta \varphi_0(x)\,\frac{dx}{x} = \frac{\pi}{2}\arctan\left[\frac{2}{\pi}\left(\ln\frac{\delta}{2} + \gamma\right)\right] + \frac{\pi^2}{4} \tag{A9}$$

Thus it is not necessary to rely on the Mathematica numerical routine for the integration about the singularity, but agreement of eq A9 with the numerical integrations of $\varphi(x)/x$ and $\varphi_0x)/x$ incidentally confirms that Mathematica does indeed handle the singularity at $x = 0$ correctly.[17]

To divide the integral for $\rho_0(x)$ in eq 11 into to two terms in the spirit of eq A7, we utilize the fact that the oscillatory numerator in $\Phi(s,x)$, approaches a finite limit:

$$\lim_{x\to 0} C(s,x) = \frac{2}{\pi}\ln s \tag{A10}$$

while $\Phi(s,x)$ and the entire integrand in eq 11 become infinite.[18] In the small increment δ we can represent this function adequately by its limiting value or, a bit more accurately, by an average

$$A(\delta,s) = \frac{1}{2}\left[\frac{2}{\pi}\ln s + J_0(\delta)\,Y_0(s\delta) - Y_0(\delta)\,J_0(s\delta)\right] \tag{A11}$$

Then, in a variation of a scheme used by Goldenberg[18,19] we write

$$\rho_0(s) = A(\delta,s)\frac{2}{\pi}\int_0^{\delta}\varphi_0(x)\,\frac{\mathrm{d}x}{x} + \frac{2}{\pi}\int_{\delta}^{\infty}\mathrm{e}^{-\sigma^2x^2}\,\Phi(x)\,\frac{\mathrm{d}x}{x} \tag{A12}$$

The first term contains nothing new, and the second is well behaved, with no singularity within the range of integration. Calculation of $\rho_0(s)$ according to eq A12 was successful with δ of 10^{-6} or 10^{-7} for all s and σ, except that for σ more than about 1000 it also became necessary to increase the number of recursive bisections of the integration intervals beyond the default value.

Equation 11 can also be written in the mathematically equivalent form

$$\rho_0(s) = \frac{2}{\pi}\int_0^{\infty}\mathrm{e}^{-\sigma^2x^2/s^2}\,\Psi(s,x)\,\frac{\mathrm{d}x}{x} \tag{A13}$$

with

$$\Psi(s,x) = \left[\frac{J_0(x/s)\,Y_0(x) - Y_0(x/s)\,J_0(x)}{J_0^{\,2}(x/s) + Y_0^{\,2}(x/s)}\right] \tag{A14}$$

The transformations in eqs A7–A12 can be applied similarly to this relation. The behavior of $\Psi(s,x)$ at small x is that of $\Phi(s,x)$: i.e. the limit $(2/\pi)\ln s$ of the numerator and essentially the same limit of the denominator. The numerical integration in this version worked well for large σ and s with one subdivision of the range at $x = 10^{-7}$.

End-segment profiles $\rho_0(s)$ for the cylinder model were obtained by combinations of the above procedures. Computation of $\rho(s,u)$ for interior segments according to eq 19 were also carried out and obviously involve nothing new. Since incorrect results were not always signaled by nonconvergence warnings (and vice versa), care was taken to check for consistency as s was varied and to confirm in selected cases that the same values were obtained by different routes.

In general, calculation of a value of the averaged segment density profile $\bar{\rho}(s)$ requires a double numerical integration indicated by eq 23 or by the approximation in eq 24. From the symmetry of both integrands, we note that it is only necessary to integrate over an octant of the plane bounded by $0 \le y \le x$ and $0 \le x \le \infty$. Although the “exponential” factor

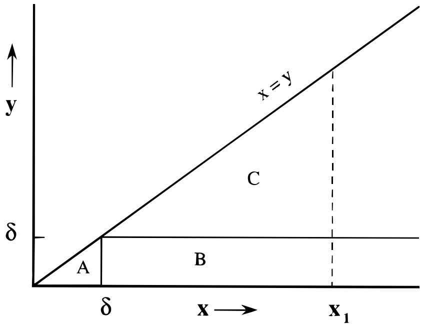

Figure 7. Schematic map of divisions of the domain of integration for two-dimensional integrals eqs 23 and 25.

$$g(x,y) = \frac{\mathrm{e}^{-\sigma^2x^2} - \mathrm{e}^{-\sigma^2y^2}}{\sigma^2x^2 - \sigma^2y^2} \tag{A15}$$

is indeterminate along the diagonal $x = y$, expansion of the exponentials shows that the value of the function is just $\exp(-\sigma^2x^2)$ along this line. For computational purposes the indeterminacy can be avoided without sensible error by stopping integration short of $y = x$, e.g. by letting $0 \le y \le 0.9999999x$. The real difficulties in the computations arise from the concentration of much of the value of the integrals around the infinity at the origin and about a line of infinities along the x-axis. It is in the context of these double integrations that partitioning of the double integrals, as discussed above for the simpler single integrals, proves to be invaluable. In Figure 7, the domain of integration for eqs 23 and 25 is shown schematically divided into regions that we consider individually.

The function $g(x,y)$ is unity at the origin on an x, y plot, and the initial slope along any direction in the x, y plane is zero. This initially “flat-top” function can, therefore, be taken as unity over a sufficiently small range, $0 \le x, y \le \delta$, of both variables. In this interval, region A in Figure 7, the integral in eq 25 reduces to

$$2I_{\mathrm{A}} = \int_0^{\delta}\int_0^{\delta} g(x,y)\,\frac{\varphi(x)}{x}\,\frac{\varphi(y)}{y}\,\mathrm{d}x\,\mathrm{d}y \approx \int_0^{\delta}\int_0^{\delta}\frac{\varphi(x)}{x}\,\frac{\varphi(y)}{y}\,\mathrm{d}x\,\mathrm{d}y = \left[\int_0^{\delta}\frac{\varphi(x)}{x}\,\mathrm{d}x\right]^2 \tag{A16}$$

The fact that the symmetry of the integrand $\varphi(x)\,\varphi(y)/xy$ allows the integral in eq A16 to be written as the square of the single integral already known from eq A9 is crucial here since, perhaps not surprisingly, direct double numerical integration with Mathematica encounters convergence difficulties near the origin, resulting in lengthy computations and results good to perhaps no better than two or three significant figures. The constancy of $g(x,y)$ near the origin makes its indeterminacy at $x = y$ in this region irrelevant.

The region labeled B in Figure 7 is a narrow strip $0 \le y \le \delta$ within which $g(x,y)$ reduces to $[1 - \exp(-\sigma^2x^2)]/\sigma^2x^2$ and the integral of $\varphi(y)/y$ is given without sensible error by the analytical result in eq A9. Thus, we separate the variables x and y, deal analytically withthe infinity in $\varphi(y)/y$, and reduce the integration from two dimensions to one:

$$I_{\mathrm{B}} = \int_{x=\delta}^{\infty} \frac{1 - \mathrm{e}^{-\sigma^2 x^2}}{\sigma^2 x^2} \frac{\varphi(x)}{x} \int_0^{\delta} \frac{\varphi_0(y)}{y} \, \mathrm{d}y \, \mathrm{d}x = \int_{\delta}^{\infty} \frac{1 - \mathrm{e}^{-\sigma^2 x^2}}{\sigma^2 x^2} \frac{\varphi(x)}{x} \frac{\pi}{2}\left[\arctan\left(\frac{2}{\pi} \ln \frac{\delta}{2} + \gamma\right) + \frac{\pi}{2}\right] \mathrm{d}x \quad \text{(A17)}$$

Since $\varphi(x)/x$ asymptotically approaches $\pi/2$, it follows that the integrand in eq 19 becomes proportional to $1/x^2$ at sufficiently large x, and it is not necessary to continue numerical integration beyond any point x_1 where this dependence prevails. A simple rule is easily established: if the increment of the integral from x_1 to $2x_1$ is twice the value from $2x_1$ to $4x_1$, the asymptotic region has been attained, and the latter increment is equal to the rest of the integral from $4x_1$ to infinity.

Finally, in region C we have to employ the general form of the integral in eq 25 and carry out the two-dimensional numerical integration:

$$I_{\mathrm{C}} = \int_{x=\delta}^{\infty} \int_{y=\delta}^{\infty} g(x,y) \frac{\varphi(x)}{x} \frac{\varphi(y)}{y} \, \mathrm{d}x \, \mathrm{d}y \quad \text{(A18)}$$

However, this domain is free of singularities, and some further simplification is possible. We recognize that $g(x,y)$ causes the integrand to be damped out more rapidly as y increases toward $y = x$ and that $\varphi(y)/y$ is also a rapidly decreasing function of y for $y > \delta$. Consequently, the integral in C is concentrated near the B−C boundary, and, as in region B, the cross-sections of the integrand at fixed x can be expected to become proportional to $1/x^2$ with increasing x. Just as in region B, the integration beyond some sufficiently large value of x can then be completed analytically. This expedient is important in limiting the time required for the integration in region C. Even so, this integration was calculation intensive, typically requiring on the order of 10^2 min to explore enough of region C to ensure results with six significant digits.

Assembling the pieces, we get $I_2(\sigma) = 2(I_{\mathrm{A}} + I_{\mathrm{B}} + I_{\mathrm{C}})$, and then from eq 24, we can calculate the approximate value of $\bar{\rho}(s)$ at sufficiently small distance s. This approximation is most useful for large σ where the applicable range of s is large.

To formulate a general procedure for calculating $\bar{\rho}(s)$ for any s and σ for the cylinder model according to eq 23, we use the framework of computations just described for $I_2(\sigma)$ with the integrand multiplied by the product of oscillatory factors from $\Phi(s,x)\ \Phi(s,y)$. The small increment δ in x and y defining region A in Figure 7 is chosen so that $g(x,y) = 1$ and $C(s,x) = (2/\pi)\ln s$ without significant error. Then for the contribution from region A we need only multiply eq A16 by $[A(\delta,s)]^2$. In region B, we can replace $[J_0(y)\ Y_0(sy) - Y_0(y)\ J_0(sy)]$ by the constant $A(\delta,s)$ and integrate $\varphi(y)/y$ according to eq A9. In this way the double integral in region B is again reduced to a single integral, and numerical integration over a line of infinities of alternating sign along the x axis is avoided. With these specifications, $\bar{\rho}(s)$ is given by

$$\bar{\rho}(s) = 2(I_{\mathrm{A}}' + I_{\mathrm{B}}' + I_{\mathrm{C}}') \quad \text{(A19)}$$

$$I_{\mathrm{A}}' = [A(\delta,s)]^2 \frac{\pi^2}{2}\left\{\arctan\left[\frac{2}{\pi}\left(\ln \frac{\delta}{2} + \gamma\right)\right] + \frac{\pi}{2}\right\}^2 \quad \text{(A20)}$$

$$I_{\mathrm{B}}' = A(\delta,s) \int_{\delta}^{\infty} \frac{1 - \mathrm{e}^{-\sigma^2 x^2}}{\sigma^2 x^2}\, C(s,x) \frac{\varphi(x)}{x} \times \frac{\pi}{2}\left[\arctan\left(\frac{2}{\pi} \ln \frac{\delta}{2} + \gamma\right) + \frac{\pi}{2}\right] \mathrm{d}x \quad \text{(A21)}$$

$$I_{\mathrm{C}}' = \frac{4}{\pi^2} \int_{\delta}^{\infty} \int_{\delta}^{\infty} g(x,y)\, C(s,x) \frac{\varphi(x)}{x}\, C(s,y) \frac{\varphi(y)}{y} \, \mathrm{d}x \, \mathrm{d}y \quad \text{(A22)}$$

Although, like the components of the calculation of $I_2(\sigma)$, these expressions are free of singularities that would pose inherent difficulties for numerical integration, the double integration over region C offers a greater computational challenge than eq A18. Rather than a monotone sloping surface, the integrand of eq A22 exhibits positive and negative regions whose exploration may require more recursive subdivisions of the integration region if contributions to the integral are not to be lost. Furthermore, the oscillatory factors $C(s,x)$ and $C(s,y)$ in the integrand make it impossible to discern an asymptotic region in which brute-force evaluation can be replaced by analytic integration. However, one corollary of the simplifying behavior described above of the double integration for $I_2(\sigma)$ still holds: although no part of the B-region or C-region integrand is now proportional to $1/x^2$, it remains true that for sufficiently large x the increment of the integral between x_1 and x_2 in the C region is proportional to the increment from the B region over the same range of x. Thus, once data suffice for an adequate estimate of the proportionality constant, an increment of the integral obtained from the relatively simple single integration in the B region can be used to calculate the value of the corresponding increment in the C region. Still, the evaluation of $\bar{\rho}(s)$ from eq 23 was sufficiently cumbersome that we pursued it only to the extent of obtaining a few values, as shown in Table 2 and Figure 3, to compare with the approximation $\bar{\rho}(s)_{\mathrm{appr}}$ from eq 24 and with middle-segment profiles.[20]

Evaluation of the average depletion layer distance s_{d} for the cylinder according to eqs 11 and 28 involves two-dimensional numerical integration over x and s. The calculation was done using a form (or forms) for the x integration that had been confirmed to give correct $\rho_0(s)$ values over the applicable range of s. In some instances results were checked by calculating s_{d} from the middle-segment profile $\rho(s,0.5)$. Although integration with respect to s causes no difficulty per se at the limit $s = 1$, it is possible to simplify the double integration in the range $1 \le s \le s_1$ where eq 16 is adequate:

$$s_{\mathrm{d}}^{\,2} - 1 = \int_1^{s_1} \left[1 - \frac{4}{\pi^2} I_{\mathrm{JC}} \ln s\right] 2s \, \mathrm{d}s\Bigr) + \int_{s_1}^{\infty} [1 - \rho(s,u)] 2s \, \mathrm{d}s) \quad \text{(A23)}$$

In any case, these were also lengthy calculations requiring on the order of 10^2 min for each value of s_{d}.

References and Notes

(1) Casassa, E. F. *Macromolecules* **1984**, *17*, 601.
(2) Casassa, E. F. *Macromolecules* **1995**, *28*, 7756.

(3) Carslaw, H. S.; Jaeger, J. C. *Conduction of Heat in Solids*, 2nd ed.; Oxford University Press: London, 1959.

(4) This qualitative characterization of the end profile probably holds regardless of the barrier geometry. See, for example, Figure 5 in ref 2, which shows how density profiles change as u is varied in steps from 0 to $^1/_2$ for linear chains at a plane interface.

(5) Jaeger, J. C.; Clarke, M. *Proc. R. Soc. Edinburgh A* **1942**, *61*, 229.

(6) The heat-flow analog of eq 14 has attracted particular interest since it gives the energy flux across the surface of a heating wire embedded in a conducting medium. See CJ, p 336.

(7) The temperature distributions plotted in Figure 41 of CJ (p 337) translate into polymer end-segment density profiles if ordinate values are subtracted from unity. The parameters labeling the curves are our σ^2. In terms of the physics of the problem, we are interested in values of σ larger than the ca. 32 upper limit of the profiles given in CJ and by Jaeger.[8]

(8) Jaeger, J. C. *J. Mathematics Phys.* **1956**, *34*, 316.

(9) From the simple change of variable $w = Tr$ which transforms the equation for radial diffusion in spherical coordinates (CJ, eq 9.1.2) into the one-dimensional form of eq A3 in the Appendix, a straightforward analogy is implied between the formalisms for chains, linear or branched, in a semiinfinite region bounded by a plane and in the region around a spherical inclusion.

(10) We note without proof that the asymptotic segment profile at large σ for a free end of a star chain near a sphere is $(1 - 1/s)$ and for an interior segment (thus for $\bar{\rho}(s)$ as well) is $(1 - 1/s)^2$—just as for linear chains.

(11) The points for the cylinder model in Figure 5 are fitted reasonably ($R^2 = 0.9993$) by a cubic expression in log σ:

$$\Delta s_{\mathrm{d}} = 0.91044 - 0.13655 \log \sigma - 0.043011(\log \sigma)^2 + 0.013757(\log \sigma)^3$$

However, this function is worthless for extrapolation in either direction beyond the span of the data: $0.1 \leq \sigma \leq 1000$. Furthermore, we must recognize the artificiality of treating calculated points of a particular function as if they are empirical data subject to random error.

(12) Casassa, E. F. *Polym. Prepr. (Am. Chem. Soc., Div. Polym. Chem.)* **1994**, *35* (1), 62.

(13) Napper, D. H. *Polymeric Stabilization of Colloidal Dispersions*; Academic Press: New York, 1983.

(14) Asakura, S.; Oosawa, *F. J. Chem. Phys.* **1954**, *22*, 1255; *J. Polym. Sci.* **1958**, *33*, 183.

(15) Wolfram, S. *Mathematica*, 2nd ed.; Addison Wesley: Redwood City: CA, 1991; pp 683−689.

(16) The integration can be accomplished by letting $x = \exp(y)$ to transform the integral to the reciprocal of a polynomial and then applying a standard form: e.g. eq 2.172 in: Gradshteyn, I. S.; Ryzhik, I. M. *Tables of Integrals, Series, and Products: Corrected and Enlarged Edition*; Academic Press: New York, 1980.

(17) Version 1.03 of Mathematica for the Macintosh did not arrive at convergent results for numerical integrations of $\varphi(x)/x$ and $\varphi_0(x)/x$ for $0 \leq x \leq \delta$, even when the depth of recursion was increased to an extent requiring computation times of several hours.

(18) Goldenberg, H. *Proc. Phys. Soc. B* **1956**, *69*, 256.

(19) For numerical calculations, Goldenberg actually used the form

$$\rho_{\mathrm{n}}(s) = \frac{2}{\pi} A(s,\delta) I_{\mathrm{JC}} + \frac{2}{\pi} \int_{\delta}^{x_1} \mathrm{e}^{-\sigma^2 x^2} \left[\Phi(s,x) - \frac{A(s,\delta)}{J_0^{\,2}(x) + Y_0^{\,2}(x)} \right] \frac{\mathrm{d}x}{x}$$

with x_1 chosen large enough to suffice in place of the infinite upper limit.

(20) Some of the calculations of $\bar{\rho}(s)$ for the cylinder model were facilitated by using Mathematica 2.2 on a Power Macintosh (8100/80). A gain in computation speed of about 9-fold was realized.

MA961185Q